
Article:
Lin, S, Wang, Q, Nikitas, N et al. (2019) Effects of oscillation amplitude on motion-induced forces for 5:1 rectangular cylinders. Journal of Wind Engineering and Industrial Aerodynamics, 186. pp. 68-83. ISSN: 0167-6105

https://doi.org/10.1016/j.jweia.2019.01.002

Effects of oscillation amplitude on motion-induced forces for 5:1 rectangular cylinders

Siyuan Lin[a, b], Qi Wang[a*], Nikolaos Nikitas[b**] and Haili Liao[a]

[a] Department of Bridge Engineering, School of Civil Engineering, Southwest Jiaotong University,Chengdu,610031, China
[b] School of Civil Engineering, University of Leeds, Leeds, LS2 9JT, UK

*wangchee_wind@swjtu.edu.cn, **n.nikitas@leeds.ac.uk

Abstract

While the 5:1 rectangular cylinder is a benchmark section, studied extensively, there are limited experimental studies commenting on any amplitude-dependence of its motion-induced forces. To this goal, such a cylinder is tested in wind tunnel through a forced vibration protocol for extracting distributed simultaneous pressure measurements under smooth flow conditions and for different heaving, pitching and coupled motion amplitudes. Ordinary flutter derivatives are extracted, and discrepancies due to oscillation amplitude are scrutinized. Spectral analysis is performed for the developing motion-induced forces, and it is found that torsional amplitudes above a threshold would increase higher harmonic frequency content. The phenomenon was also confirmed by means of Probability Density Functions and (PDFs) the Proper Orthogonal Decomposition (POD) of the unsteady wind force. In order to understand the link between the observed amplitude dependence and the flow field variation, the movement of the reattachment point on the cylinder surface is investigated by interpreting statistics of the recorded pressure measurements. The response in terms of instantaneous angle of attack is proven to be incompatible with respect to observations, since equal amplitudes of this variable result to different motion-induced forces.

Keywords: motion-induced force; 5:1 rectangular cylinders; forced-motion tests; spectral analysis; statistical analysis

1. Introduction

Due to the fundamental geometry of rectangular cylinders with aspect ratio of 5:1, a great number of researches have been conducted concerning their aerodynamic properties. Under the framework of BARC (Benchmark on the Aerodynamics of a Rectangular 5:1 Cylinder, Bartoli et al, 2008), Bruno et al (2014) investigated aerodynamic forces, their spanwise correlations, and their sensitivity to flow unsteadiness have all been investigated through wind tunnel tests and/or Computational Fluid Dynamics (CFD) simulations. Namely, Matsumoto et al (2001) tried to explain the mechanism of highly coherent structures in surface pressures, for the spanwise direction, through stationary wind tunnel tests. They found that the coherence of the aerodynamic force is higher than that of the approaching flow, and stressed that the pressure fluctuations at a position slightly upstream than the reattaching point would critically influence the evaluation of the buffeting force. For estimating the reattachment point location, pressure data without any flow field visualizations were employed. Le et al (2009)) extended the work by studying the temporal-spectral coherent structures of the wind pressures using both Fourier and wavelet analysis. Similarly, statistical characteristics of pressures on the stationary 5:1 rectangular cylinder in both smooth and turbulent flow were summarized (Ricciardelli and Marra, 2008).

Besides the research on stationary models, results from oscillating rectangular cylinders are necessary to shed light on the characteristics of the motion-induced force components. The state of motion cannot be fully controlled in free vibration tests, so researchers have adopted forced-vibration tests to

better investigate aeroelastic characteristics. As in the case of classical flutter-induced motion on elongated rectangular cylinders(B/D=25, with B the cross section width and D the depth facing the flow), the post-critical flutter response is characterized by large amplitude oscillations, especially in terms of rotational component (Pigolotti et al, 2017). Information solely on the displacement response of a model could not contribute significantly to the understanding of the complex aerodynamics at the micro scale (i.e. separation and vortex formation processes); therefore additional measurements should be conducted on the pressure field. Beyond a few forced motion tests for 5:1 rectangular cylinders, pressures of rectangles with aspect ratio of 6.67:1 under imposed heaving and small pitching motion were measured in both smooth and turbulent flow (Haan et al, 2016). The motion-induced forces were investigated through the ordinary flutter derivatives' theory (Scanlan, 1978). By combining and comparing the pressure amplitudes and the phase lag between pressures on the top surface and the displacement, changes of flutter derivatives were tracked back to a turbulence-induced increment of the curvature of the separated shear layers and the upstream movement of the reattachment point. Compared with Haan et al's research, Noda et al (2003) investigated the amplitude effect on flutter derivatives of very thin rectangular cylinders with B/D=13 and 150. A_2^* is strongly affected by the torsional amplitude; this was attributed to the movement of the flow separation on the cylinder surface. In principal, flutter derivatives are based on the combination of the small-amplitude hypothesis with the aeroelastic-force linearization. However, several researchers during wind tunnel tests of particular bridge decks have observed wind forces consisting of high order motion harmonics (Diana et al, 2008; Falco et al, 1992; Lee and Su, 2015; Mannini et al, 2016). This implies the existence of nonlinearity in motion-induced forces and, at some level the invalidation of the flutter derivative notion. Such nonlinear characteristics were considered in different models, which were applied to flutter response predictions. Next work on the nonlinearity of motion-induced forces was carried out through CFD analyses, particularly for flat plate and H-sections (Lin and Haili, 2013; Tang, 2015). For these cases, a secondary vortex has been identified as a potential source of the nonlinear harmonic content. However, the applicability of this finding to more typical bluff sections, like a 5:1 rectangle, needs to be verified with wind tunnel tests.

Clearly, researchers have long identified that flutter derivatives are amplitude dependent, with several publications having reported such views (Chen et al, 2005; Diana et al, 2004; Kareem and Wu, 2016; Noda et al, 2003; Sarkar et al, 2009; Washizu et al, 1978; Wu et al, 2013). The goal of the present research is to investigate experimentally and describe in more detail any amplitude effects on the motion-induced forces of a 5:1 rectangular cylinder. Therefore, a forced test rig was designed to facilitate large amplitude heaving and pitching motions of sectional models. Typical testing cases, by means of different motion amplitude ranges, were selected to uncover changing characteristics of the recorded motion-induced forces. Detailed analysis, considering the in-parallel evolution of motion and surface pressures, was carried out to reveal the inherent flow mechanism substantiating the apparent nonlinearity.

In the next section, the details of the wind tunnel test set-up and the experimental cases considered are described. The characteristics of the motion-induced force are analysed in section 3, while section 4 discusses the inherent flow mechanism linking to the nonlinearity of the aeroelastic forces. Finally, the amplitude dependence of motion-induced forces on 5:1 rectangular cylinders is summarized, trying to propose explanations and extensions associated with a possible flow mechanism.

2. Wind tunnel tests

2.1 Experimental set-up

These wind tunnel tests were conducted in the second test section of the XNJD-1 wind tunnel, a closed-circuit, low-speed wind tunnel located in the Southwest Jiaotong University, China. The test section has width and height of 2.4m and 2m, respectively. The wind speed can be adjusted from 1m/s to 45m/s. The quality of the flow field is very stable, and the longitudinal and transversal turbulence intensity of the empty wind tunnel is less than 0.5% on average according to its performance report (Zhou et al, 2003). The rectangular model used in the forced motion tests is the same as the one

mentioned in Li et al (2016). The model is made of glass fibre reinforced by transverse ribs to achieve very sharp edges and smooth surfaces. It has a depth, D, of 0.1m, a streamwise width, B, of 0.5m and a span, l, of 1.5m. Screws were used to fix the top face of the model in place, for allowing the installation of pressure taps and connection tubes. The blockage ratio at zero angle of attack is approximately 3.1%. Two identical end plates (0.8m wide and 0.265m high) are installed on both sides of the cylinder to enable a close to bi-dimensional flow filed.

Fig. 1 Partial view of XNJD-1 wind tunnel

The distribution of pressure rings and pressure taps in one section is shown in Fig. 2. Although there are 7 rings of pressure taps along the model, only the pressure ring D near the middle of the cylinder is chosen for analysis. Referring to previous research (Xiong, 2017), spanwise correlation coefficients were found to increase at larger oscillation amplitudes. Therefore, albeit such test has not been carried out in the present study, the measurements on the middle pressure ring may be considered sufficient for inferring the amplitude dependences of the motion-induced forces.

The pressure measurement system shown in Fig. 3 is the type DSM 3400 Scanivalve combined with the ZOC 33/64PxX2 pressure measuring module, which has 64 sensors to measure the pressure time histories. The length of the pressure tubes were all made 0.2m to ensure good frequency response characteristics (Cunming, 2007). The recording time and sampling frequency were set to 64s and 128Hz respectively.

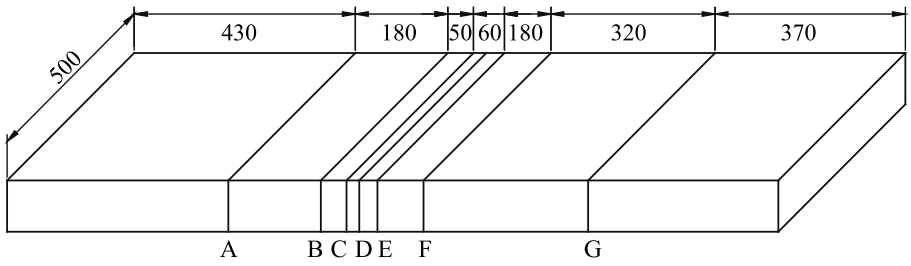

(a)

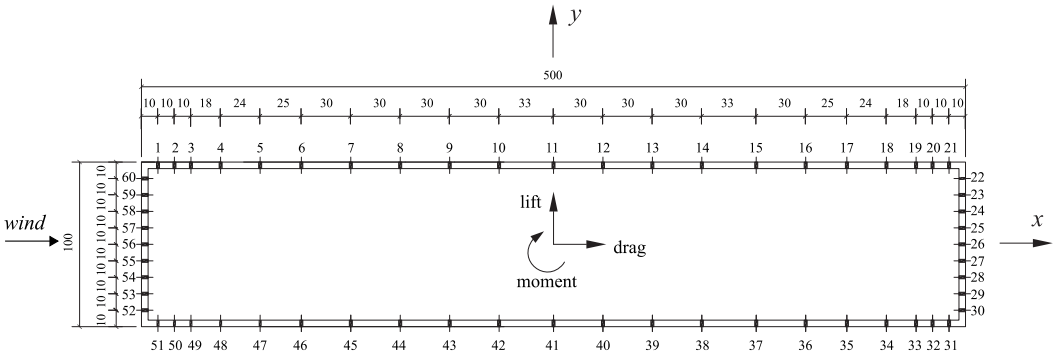

(b)

Fig. 2 (a) Layout of the pressure ring on the model (mm) (b) Layout the pressure taps in one section (mm)

A schematic diagram of the forced motion test rig is shown in Fig. 4, while its detailed description can be found in (Li et al, 2016). Some improvements have been made so that torsional amplitude can range from 0.1° to 45° and the heaving amplitude could span from 1mm to 200mm. The driving frequency varies from 0.1Hz to 3Hz. Also, coupled motion of pitching and heaving with different phase lag can be achieved. The displacement of the model was measured with two laser displacement sensors (Micro-Epsilon optoNCDT1401). The sensors measured the displacement of the front edge and the midpoint at pressure ring D. The model tested is shown in Fig. 5. In the case of motion with only pitching component, displacements are directly transformed into a rotation angle. Synchronization of pressure and displacement sampling was achieved by a software trigger of both measuring systems; this reaches a time delay below 5ms. Therefore, phase lags between pressure and displacement induced by initiation errors could be neglected.

Fig. 3 DSM 3400 pressure measurement system

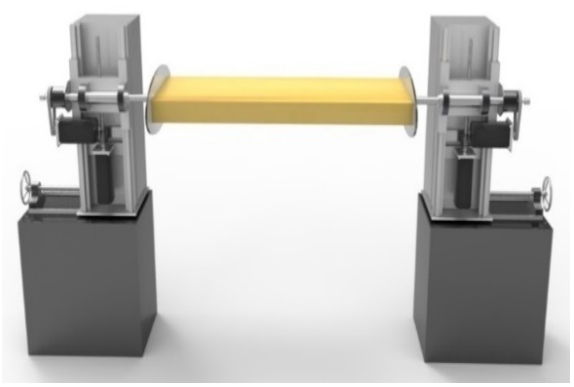

Fig. 4 Schematic diagram of forced motion test rig

Fig. 5 Forced motion wind tunnel test along with pressure measurement

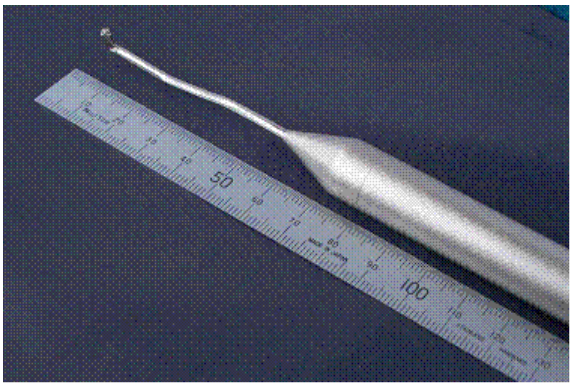

Fig. 6 Cobra probe for measuring wind speed

The velocity of the incoming flow was measured using both a TFI Cobra Probe (shown in Fig. 6) and a Pitot tube placed at 2m distance in front of the model.

2.2 Testing cases

Compared with previous researches (Haan et al, 2016; Li et al, 2016; Sarkar et al, 2009), the cases of large amplitude single pitching and single heaving motion, as well as coupled motion, were considered in this test campaign . The amplitude of single pitching motion α_0 ranges from 2° to 16°, while the single heaving amplitude h_0 ranges from 3mm to about 27mm (corresponding to h_0/B from 0.6%to 5.5%). In this step, no phase lag between heaving and pitching motion was exerted on the coupled motion tests. The heaving amplitude of 16.5mm is combined with 4 different values of pitching amplitudes (2°, 5°, 10° and 14°). According to the definition of reduced wind velocity $U_r=U/fB$, any set value can be achieved by varying both U and/or f, i.e. the incoming flow velocity and forced motion frequency. Considering the limitations of the apparatus, the oscillation frequency was set between 1Hz and 2.5Hz and wind velocity ranged from 7.5m/s to 15m/s. Thus, reduced wind velocities between 6 and 32 were accomplished. Pressure distributions of the stationary cylinder at 0° angle of attack in all tested wind velocities were also measured for comparison purposes.

The whole tests are performed in Reynolds number ($Re=UD/v$, with D denotes the depth of the model) range of 5×10^4 ~1×10^5. For the 5:1 rectangular cylinder, the frequency of vortex shedding is given by a Strouhal number ($St=f_vD/U$) of St=0.11, which is rather insensitive to Reynolds number effects (Schewe, 2013). This translates to vortex shedding frequencies of 1.1*U Hz. The value of wind velocity and forced motion frequency in the experiment was selected in order to foster the separation of the vortex- and motion-induced force components.

3. General characteristics of motion-induced force

3.1 Extraction of motion-induced forces

Having surface pressures along the cylinder, lift, drag and moment exerted on the model could be derived through integration assuming a full spanwise correlation. Drag, for 5:1 rectangular cylinders shows different characteristics from lift and moment (Xu et al, 2016), with the 2nd order harmonic being able to dominate the spectrum of its motion-induced part. A detailed investigation of the motion-induced drag would also require forced-motion capability in the along-wind direction, which the current set up cannot enable. Thus, any drag related references are excluded from any further discussions within the article.

The wind force in general is the sum of mean ($\overline{F}$) and fluctuating components. The fluctuating components consist of vortex-induced (F_v), motion-induced (F_{se}) and high-frequency noise (F_{noise}) force counterparts

$$F_{total} = \overline{F} + F_v + F_{se} + F_{noise} \tag{1}$$

For these test cases, the mean wind force could be easily removed by subtracting any mean offsets, while motion-induced force can be extracted by adopting a low pass filter with minimum phase distortion. As shown in Fig. 7, the broadband vortex-induced part alongside the high-frequency noise can effectively be removed from the Power Spectral Density (PSD) of lift after the filtering process (low pass frequency at 15Hz). The broadband character of the vortex shedding associated lift is thought to surface due to the distorting interactions with the imposed low frequency motion (Matsumoto et al, 2005).

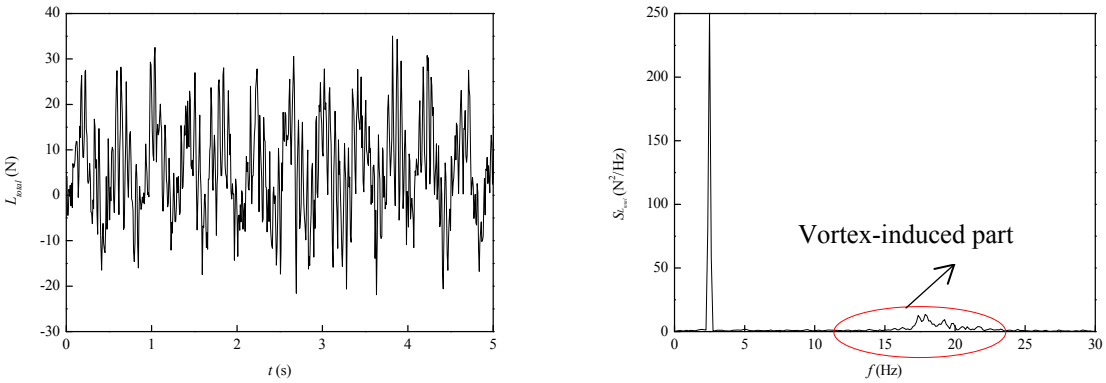

(a) Total lift and associated PSD

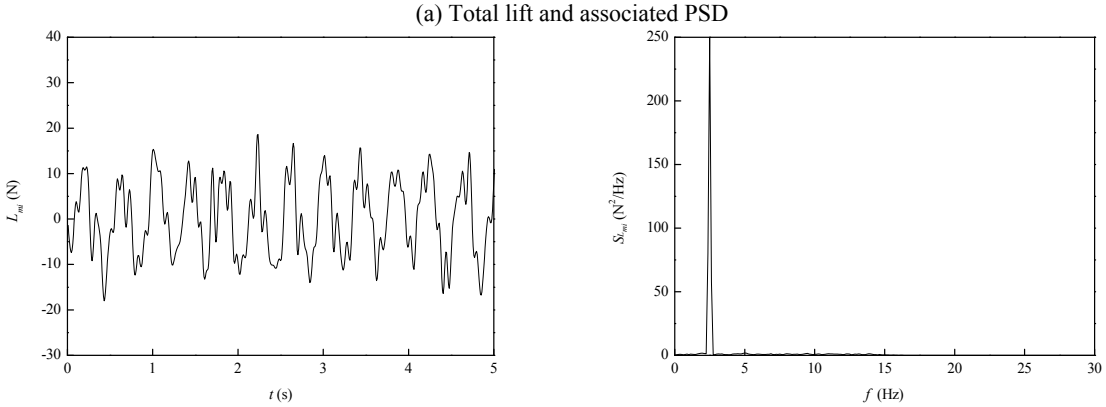

(b) Motion-induced lift and associated PSD

Fig. 7 PSD of lift force (U_r=12, single heaving, motion frequency 2.5Hz)

3.2 The amplitude dependence of flutter derivatives

Traditionally, flutter derivatives are used to model the motion-induced force for bridge decks and bluff sections. With the motion-induced force extracted from section 3.1, the flutter derivatives (A_i^*, H_i^*,i=1~4) could be derived easily referring to the theory of Scanlan (1978) through the simultaneous records of the displacement time histories. The motion-induced lift, L_{se}, and moment, M_{se}, at time t are,

$$L_{se}(t)=\frac{1}{2}\rho U^2(2B)\left[KH_1^*(K)\frac{\dot{h}}{U}+KH_2^*(K)\frac{B\dot{\alpha}}{U}+K^2H_3^*(K)\alpha+K^2H_4^*(K)\frac{h}{B}\right] \quad (2)$$

$$M_{se}(t)=\frac{1}{2}\rho U^2(2B^2)\left[KA_1^*(K)\frac{\dot{h}}{U}+KA_2^*(K)\frac{B\dot{\alpha}}{U}+K^2A_3^*(K)\alpha+K^2A_4^*(K)\frac{h}{B}\right] \quad (3)$$

where ρ is the air density, α is the pitching motion, h is the heaving motion, K is the reduced frequency and overdots represent the time derivative. The reduced frequency can be calculated by, $K=2\pi fB/U$.

For the single pitching and heaving motion cases, the torsional and heaving displacement, respectively, are harmonic functions with the same frequency f,

$$\alpha(t)=\alpha_0\cos(2\pi ft) \quad (4a)$$

$$h(t)=h_0\cos(2\pi ft) \quad (4b)$$

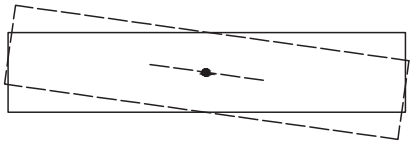

free vibration results on A_2^* and A_3^* at the initial amplitude of α_0=1.72° are close, yet not identical, to Matsumoto's and are omitted.

Fig. 9 shows flutter derivatives at different pitching amplitudes from 2° to 16°. It can be seen that H_2^* and H_3^* are relatively insensitive to amplitude effects. However, the trend of A_2^* and A_3^* versus reduced wind velocity is clearly amplitude dependent. This is similar to the findings for thin rectangular cylinders (Noda et al, 2003), where the A_2^* is strongly affected by torsional amplitude. Similar trends can also be verified by extracted flutter derivatives in full-scale for a real instability-prone bluff bridge (Nikitas et al, 2011).

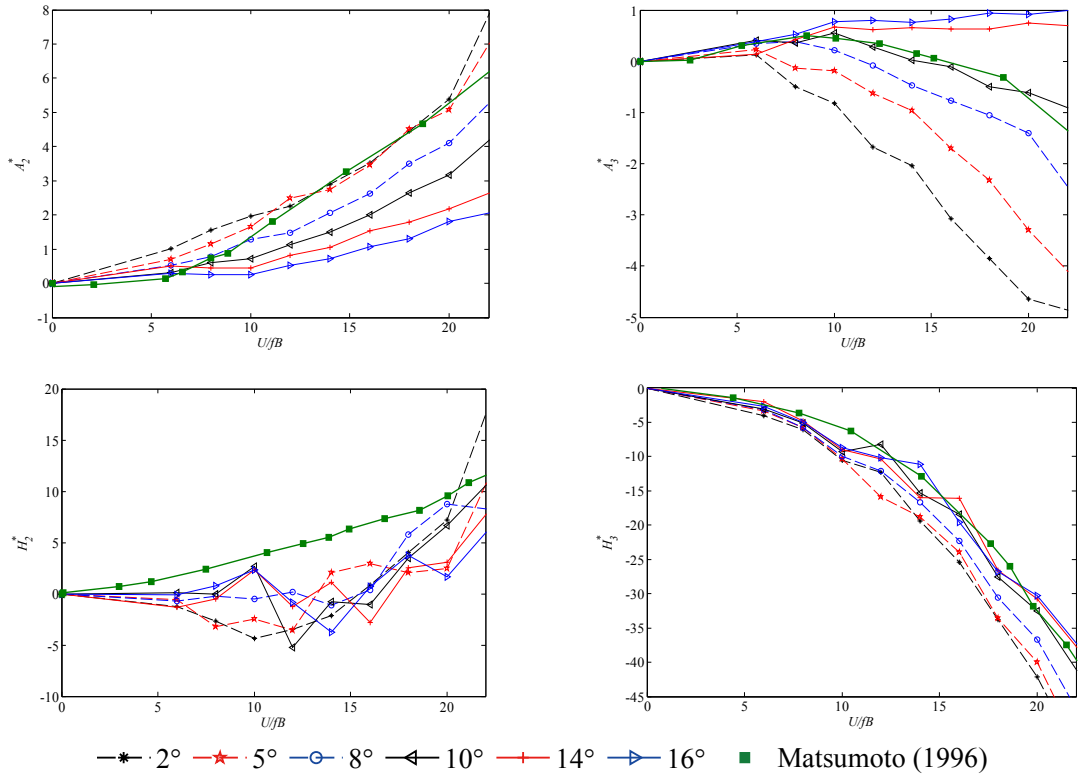

Fig. 9 Flutter derivatives of 5:1 rectangular cylinder under different amplitudes of pitching motion

Compared with Matsumoto's results, green square dots in Fig. 9, flutter derivatives for similar torsional amplitude in these experiments fall within an acceptable distance if one considers the difference of the associated setups in terms of turbulence intensity, Reynolds number and pressure tap arrangements. Particularly for turbulence intensity variations, there is a marked influence of this variable on flutter derivatives (Haan Jr, 2000). The present experiments are also performed in a larger testing section of a closed circuit wind tunnel, which differs to Matsumoto's (blockage 3.1% here against >4%). In any case, with the focus herein being the relative effect of forced amplitude on flutter derivatives, and with trends being similar to both studies, results are considered both consistent and sufficient.

For both A_2^* and A_3^*, lower absolute values are found for higher amplitude torsional motion at the same reduced velocities. According to Eq. (6a), the changing of flutter derivatives is caused by the variations of M_0/α_0 and of $\sin\phi_M$. Fig. 10 shows the cosine and sine values of the phase lag ϕ_M when α_0=2° and α_0=16°. As the difference for $\cos\phi_M$ and $\sin\phi_M$ are not significant for these two far apart torsional amplitudes, the decrement of M_0/α_0 would contribute more to the lower value of A_2^* and A_3^*. As a series of reduced wind velocities were tested in this study, the amplitude dependence will be only showcased from this point onwards for the case of a single reduced wind velocity of U_r=6. Results are similar also for other U_r values, which are not presented herein for the sake of brevity.

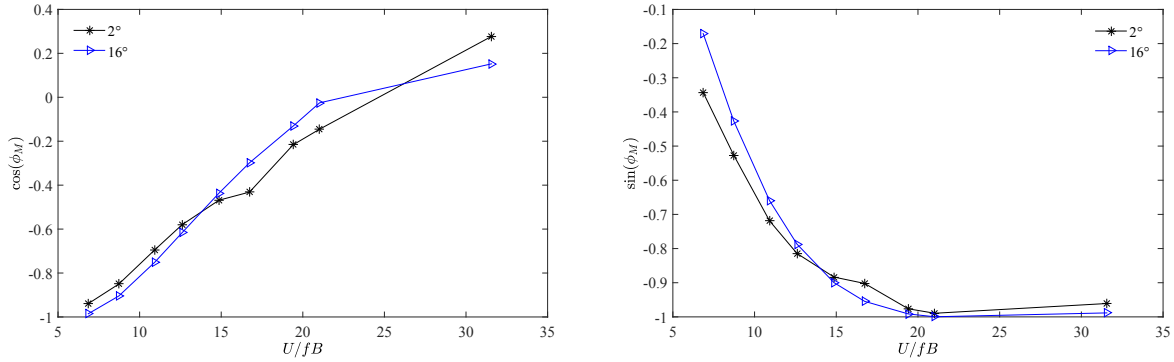

(a) (b)

Fig. 10 (a) phase lag (b) cosine and (c) sine value of phase lag between motion-induced moment and displacement

3.3 Spectral characteristics of motion-induced forces

Based on the discussion in the previous section, the FFT technique is adopted to investigate the spectral properties of the motion-induced lift and moment for the 5:1 rectangular cylinder when in harmonic motion. In that case, the critical condition where Scanlan's linearized assumption (single harmonic input resulting single harmonic output) is applicable could be found. For the simplicity of the following discussion, the motion-induced lift and moment are transformed into lift and moment coefficients by,

$$C_L = L_{se} / (\frac{1}{2}\rho U^2 B) \tag{8a}$$

$$C_M = M_{se} / (\frac{1}{2}\rho U^2 B^2) \tag{8b}$$

For comparison purposes, the PSDs of motion-induced lift and moment coefficients (at U_r=6, Re=5×10^4) are normalized by their variance. As shown in Fig. 11, the 1st order harmonic (same frequency as the motion frequency f_h=2.5Hz) dominates the spectra of motion-induced lift and moment coefficients, regardless of heaving amplitude. The increment of the heaving amplitude would also increase the PSD amplitude at the motion frequency coordinate. There is no higher order harmonics in the PSD of heaving cases, indicating that the Scanlan's assumption mentioned earlier applies without any question.

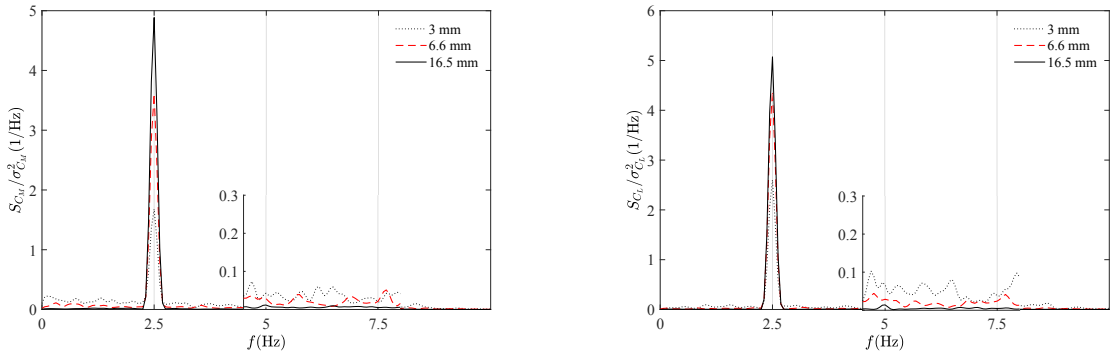

(a) (b)

Fig. 11 PSD of heaving motion-induced (a) moment and (b) lift coefficient (U_r=6)

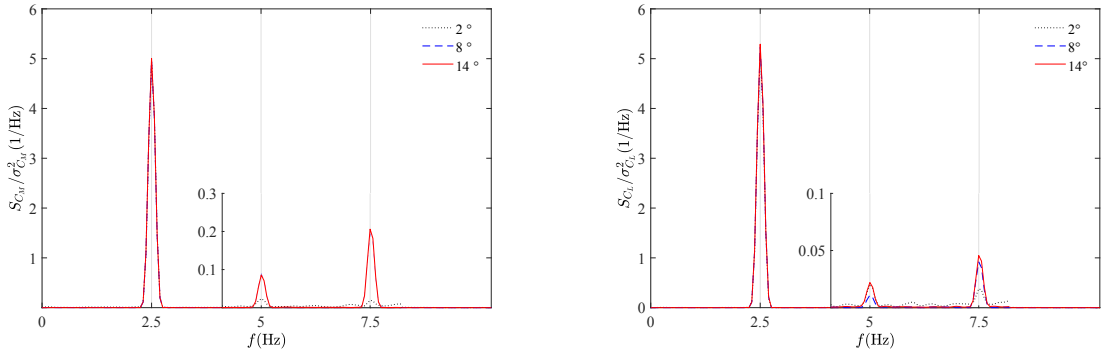

(a) (b)

Fig. 12 PSD of pitching motion-induced (a) moment and (b) lift coefficient (U_r=6)

Differently from the heaving case, the PSDs of motion-induced lift and moment coefficients under single pitching motion show a different pattern. Higher order harmonic components begin to appear in the relevant PSDs. Actually, the 3rd order component is stronger than the 2nd order one. For the PSD of motion-induced moment, the amplitude of each harmonic increases with the amplitude of pitching. Namely, the 2nd and 3rd harmonics of motion-induced moment coefficient at α_0=8° and 14° are at the same, substantially higher than the one at α_0=2, level. This is also the case for the 3rd harmonics in motion-induced lift.

Referring to the concept of total harmonic distortion (THD) (Fuchs and Masoum, 2011), the energy ratio is proposed as in Eq. (9) in order to quantify the influence of oscillation amplitude on higher harmonics. This writes as,

$$E_{Ri} = \int_{f_{1i}}^{f_{2i}} \frac{S(f)}{\sigma^2} df \times 100\% \tag{9}$$

where E_{Ri} is the energy ratio for i^{th} order harmonic, $S(f)/\sigma^2$ is the normalized PSD of motion-induced force coefficient, and f_{1i} and f_{2i} are lower and upper frequencies fully encompassing the harmonic component of interest.

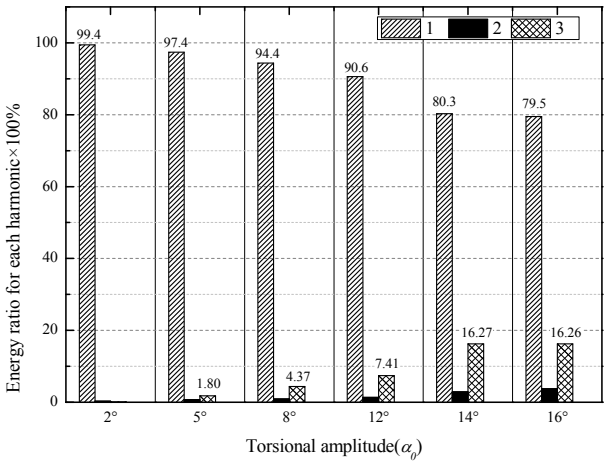

Fig. 13 Effect of amplitude on E_{Ri} for motion-induced moment in single pitching case (U_r=6)

From Fig. 13, the energy ratio of the 1st order harmonic is decreasing as the pitching amplitude is increasing. When α_0=16°, E_{R1} reduces to 79.5%, which is nearly 20% less than the ratio at α_0=2°. Obvious 3rd harmonic content (considered at over E_{Ri}> 3%) is observed when the pitching amplitude is no smaller than 8°. As such, α_0=8° can be seen as a threshold value, determining whether considerable higher harmonic energy distribution is observed in single pitching motion cases. The decline of energy ratio for the 1st order harmonic could be also behind the decline of A_2^* at larger torsional amplitudes, since M_0 in Eqs. (6), (7) is the motion-induced moment at the motion frequency alone.

When the single pitching and heaving motions are combined, nonlinear characteristics of motion-induced force for coupled motion cases (no phase lag between the two motion components) can be found. From Fig. 14, the appearance of higher order harmonics is again evident. Within the normalized PSD of motion-induced moment coefficient, 3rd order harmonic content is stronger in the case of larger torsional amplitudes. Conversely, the 2nd order harmonic of both motion-induced moment and lift coefficients at α_0=2° are larger than the ones at 8° and 14°. This is probably the most interesting aspect owning to the addition of heaving to single pitching cases. Within the PSD of motion-induced lift coefficient, the larger torsional amplitude would not translate to a higher peak at the 3rd harmonic coordinate. As seen in Fig. 15, the 3rd harmonic content appearance criterion falls to α_0=5° from the earlier α_0=8° of single pitching cases, with a subsequent saturation behaviour. All these observations indicate that the coupled motion cases are rather different, in terms of nonlinear aspects, to single motion ones requesting for a different treatment and study

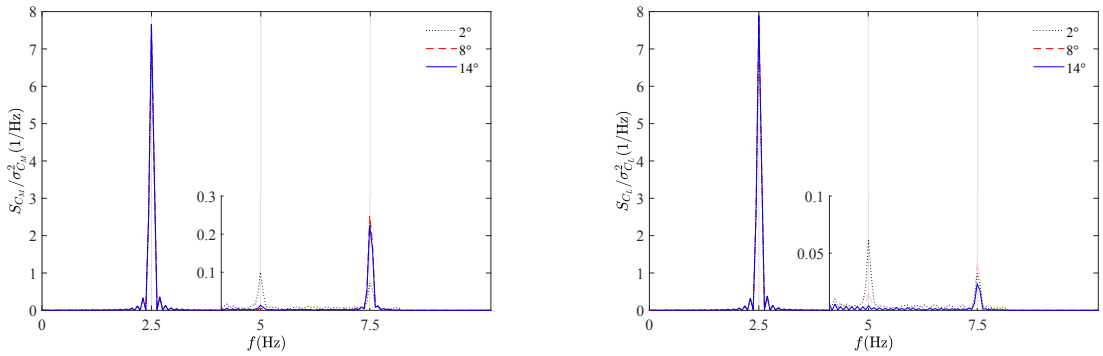

Fig. 14 PSD of coupled motion-induced (a) moment and (b) lift (U_r=6, h_0=6.6mm)

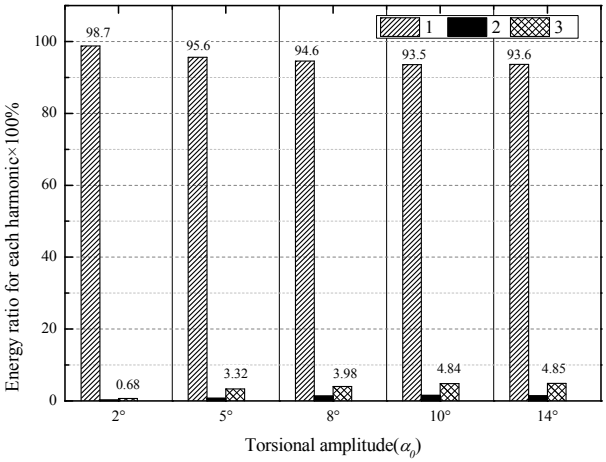

Fig. 15 Effect of amplitude on E_{Ri} for motion-induced moment in coupled motion case (U_r=6, h_0=6.6mm)

3.4 Probability density function of motion-induced forces

Fig. 16 to Fig. 18 show the PDFs of motion-induced lift and moment coefficients for the corresponding cases in Fig. 11 to Fig. 14. An indicative Gaussian distribution (in grey dashed line) is included in each figure for comparison. The lift and moment from equivalent stationary model tests were also processed into PDFs (in solid blue lines) and are shown in all figures.

In the single heaving case, the PDFs of motion-induced lift and moment coefficient are quite close to the Gaussian distribution when the heaving amplitude is lower than 6.6mm. As the heaving amplitude increases beyond 6.6mm, the distributions become bimodal. For the pitching and coupled motion

cases, the motion-induced lift and moment coefficients are far from the Gaussian distribution, showing at all times bimodal features. As the higher order harmonics take a larger part in the ensemble of the motion-induced force, the peak values of the PDFs decrease while also reshaping. From the comparison of Fig. 16, Fig. 17 and Fig. 18, it can probably be supported that the PDFs for the coupled motion case are influenced more strongly by the pitching motion, showing qualitative similarities in their associated evolutions with increasing pitching amplitudes.

Commonly for all motion cases, the increment of amplitudes results to more pronounced bimodality within the PDFs of motion-induced lift and motion coefficients. Referring to the case of a stationary 5:1 rectangular cylinder (Schewe, 2013), the variation of such lift and moment PDFs should well represent different flow patterns around the tested cylinder. Note the non-symmetric character of the produced PDFs almost at all instances. This finding was previously reviewed by Bruno et al (2014), see their Section 4.2.2, who quoted as reason for this "unexpected" symmetry breaking phenomenon testing details beyond possible misalignments of the section model. Such can be the space-wise inhomogeneity of the flow, the Pitot tube positioning, the finite nature of the time series used during the calculation of the PDFs and model imperfections (sharp corners, pressure taps). The phenomenon could as well be an inherent one, reminiscent of the symmetry breaking features appearing in the case of dynamically tested inclined circular cylinders (Nikitas and Macdonald 2015).

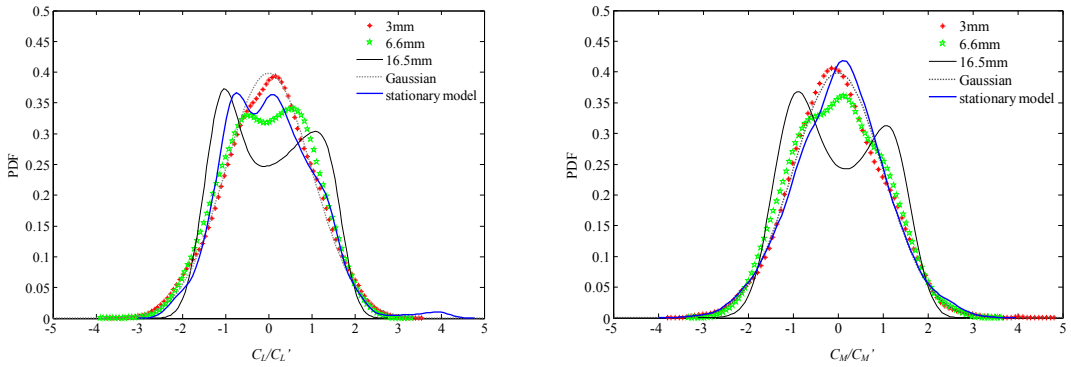

Fig. 16 PDF of heaving motion-induced lift and moment coefficient (U_r=6)

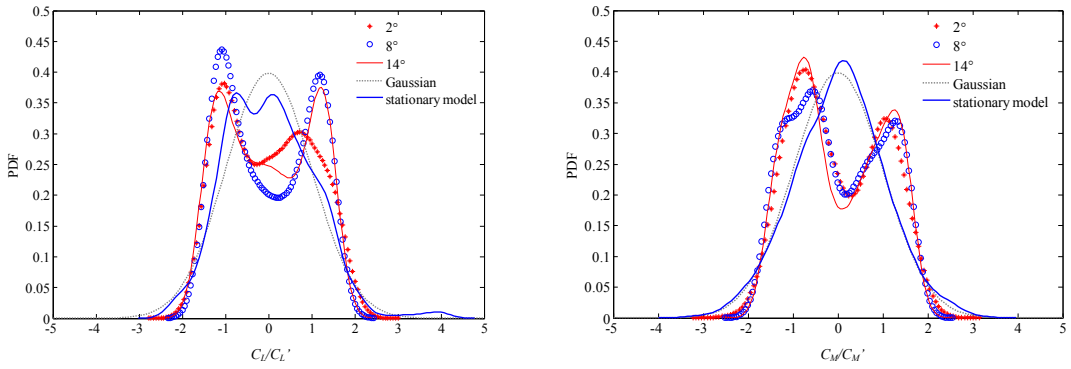

Fig. 17 PDF of pitching motion-induced lift and moment coefficient (U_r=6)

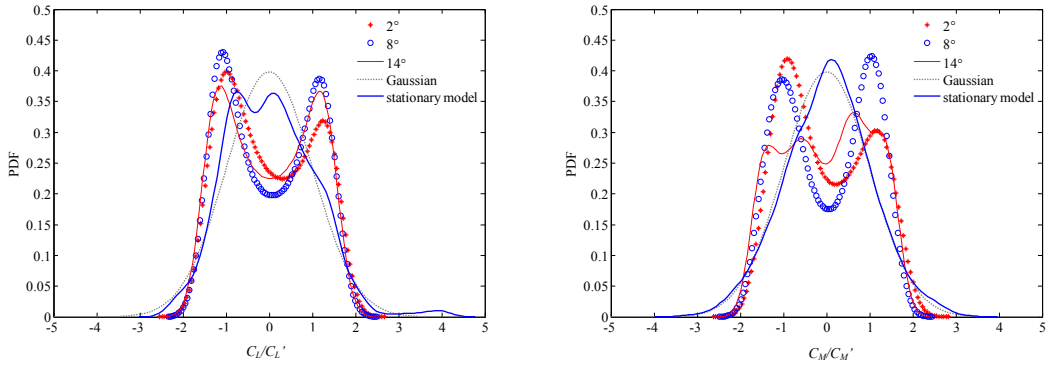

Fig. 18 PDF of coupled motion-induced lift and moment coefficient (U_r=6, h_0=6.6mm)

4. Pressure distribution and possible flow mechanism

In the previous section, the general characteristics of motion-induced force were analyzed and summarized. It is found that the pitching motion amplitude has large influence on the motion-induced force, which is inconsistent with the assumption of Scanlan's theory. The amplitude dependence of motion-induced force has been mentioned by several other researchers, but few of them try to set up a link between the flow structures and the motion-induced forces of oscillating 5:1 rectangular cylinders. Noda et al (2003) pointed out that the variation of A_2^* with the increment of torsional amplitude is linked to the movement of the reattachment point of the separated flow when researching on rectangular cylinders with B/D=13 and 150. So far, few further investigations were reported on this issue. As the pressure fluctuation is closely related to the variation of vortex structures on the cylinder surface, the mean and r.m.s values, spatial-temporal pressure coefficient distribution and POD mode of pressure coefficients will all be discussed in this part. The pressure is by $\rho U^2/2$ hence considering pressure coefficients.

4.1 Mean and r.m.s distribution of pressure

Fig. 19 shows the mean and r.m.s. value of pressure coefficient distribution under different amplitudes of pitching, heaving and coupled motion, when U_r=6. The horizontal coordinate x/B (normalized by the width of the model) represents the relative distance for each tap on the top surface from the leading sharp corner. The pressure distributions of a stationary rectangular cylinder at 0° angle of attack of angle in smooth flow are also presented for comparison. C_P and C_P' stand for the mean and r.m.s pressure coefficient for the oscillating cases, while the C_{P0} and C_{P0}' stand for the corresponding stationary cases.

For the pitching cases, the C_P and C_P' deviate from the stationary one more when the pitching amplitude increases. The peak of C_P' is increasing and moving towards the leading edge with the increment of pitching amplitude. The maximum of C_P' (α_0=14°) can reach as high as nearly 1.1, which is much larger than the value of C_P'=0.22 at α_0=2°. The local extreme of C_P is also increasing and moving towards the leading edge. One thing to notice is that C_P' begins to show the increasing trend in the trailing edge.

In terms of the heaving cases, the C_P distribution is very close to the stationary case while C_P' is higher than the stationary one with the similar trend across the top surface. For the coupled motion case, the pattern of C_P and C_P' distribution follows the same pattern as the pitching case. The combination of heaving motion has lowered the negative mean pressure coefficient.

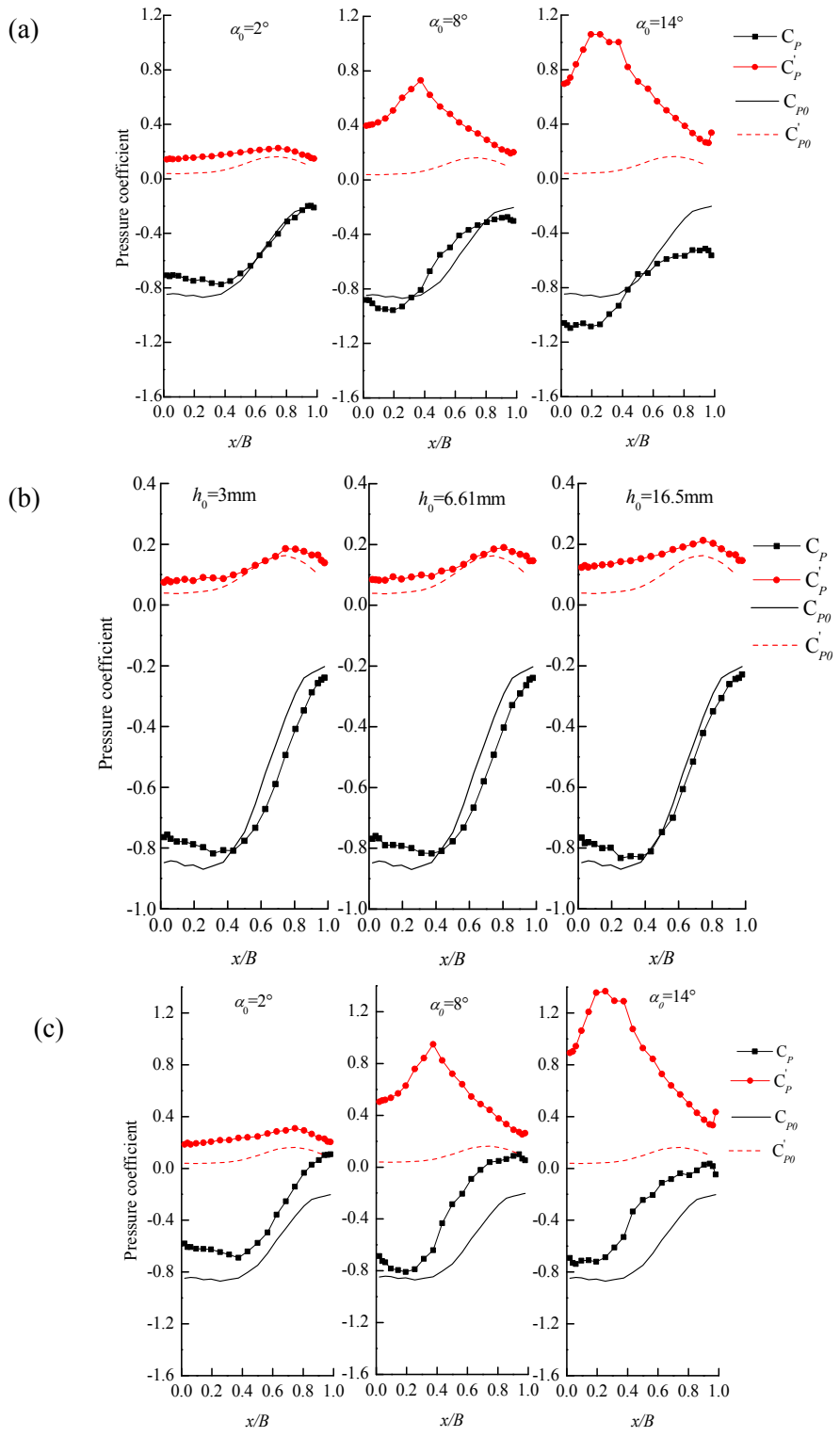

Fig. 19 Pressure coefficient distribution on the top surface of the rectangular cylinder under different oscillation amplitude (a) pitching motion (b) heaving motion (c) coupled motion h_0=6.6mm

Usually, the flow would separate in the leading edge corner of the bluff body. The 5:1 rectangular cylinder falls into the range 3.2<*B*/*D*<7.6 for which the free shear layers would reattach to the trailing edge periodically in time and form a regular vortex street in the wake (Nakamura et al, 1991; Parker and Welsh, 1983; Stokes and Welsh, 1986). The position of the reattachment point (x_R, the distance

from the leading edge) can be determined by PIV techniques or smoke and/or oil flow wind tunnel tests, which can visualize the flow. It has been verified that the mean flow reattachment point lies between the position where there is a peak in the r.m.s. of the pressure coefficients and a peak in the mean pressure (Robertson et al, 1978). Due to the lack of any more detailed flow visualizations, the reattachment point at the top surface of the section was herein assumed to coincide approximately with the mid distance between the peak of the mean and the r.m.s. of the pressure coefficients. This is close to what Mannini et al (2017) essentially proposed in their research (using the apparent peaks of the mean pressure coefficient only). With these in mind, the position of the mean reattachment point under different oscillating cases can be extracted as in Fig. 20.

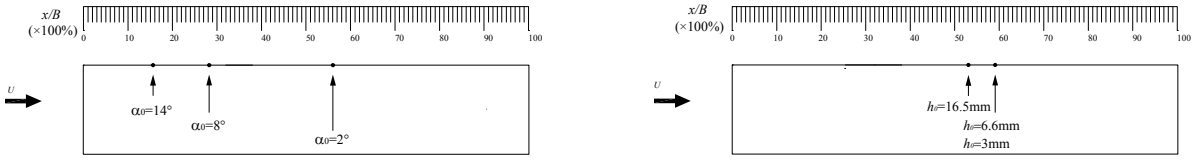

(a) single pitching and coupled motion cases (b) single heaving cases

Fig. 20 Position of the mean reattachment point on the top surface

From Fig. 20, it can be seen that the increase of pitching amplitude would make the reattachment point move towards the leading edge. Addition of the single heaving motion case has no contribution to the movement of the mean reattachment point. However, the value of x_R is quite close regardless of the heaving amplitude (varying from 3mm to 16.5mm). The early reattachment on the top of the surface would provide possibility for the further evolvement of the vortex, which may be related to the higher harmonics in the PSD. The reattached vortex may separate and reattach to the top surface again. Comparing with the flow visualizations reported in Mannini et al (2010), the sharp increase of fluctuating pressure immediately before the trailing edge, observed for the α_0=8° and 14° in single pitching and coupled motion case, is an evidence of a small counter-rotating secondary bubble. This phenomenon was also observed in the CFD investigation of flat plate (B/D=200) under large pitching amplitudes in the paper of Tang (2015). Similarly, the 5:1 rectangular cylinder under large amplitude pitching motion would present a secondary mechanism of vortex shedding.

4.2 Spatial-temporal distribution of pressure coefficients

(a)

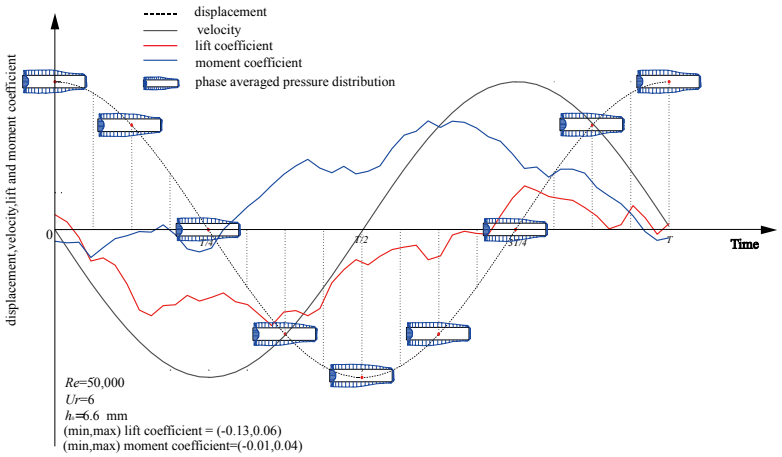

(b)

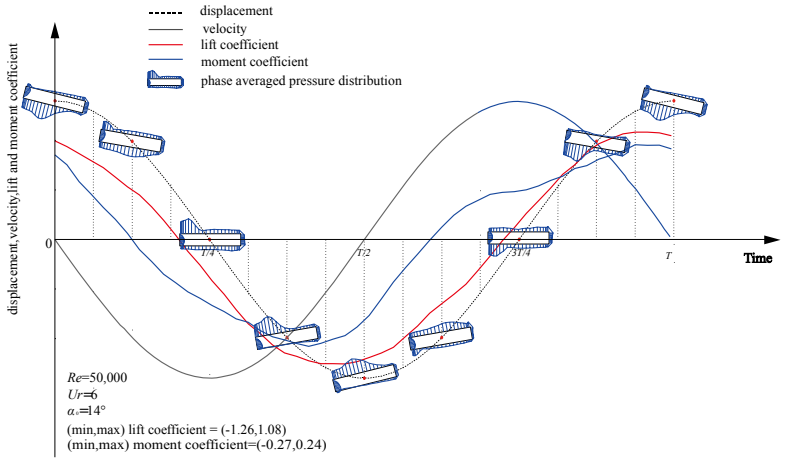

(c)

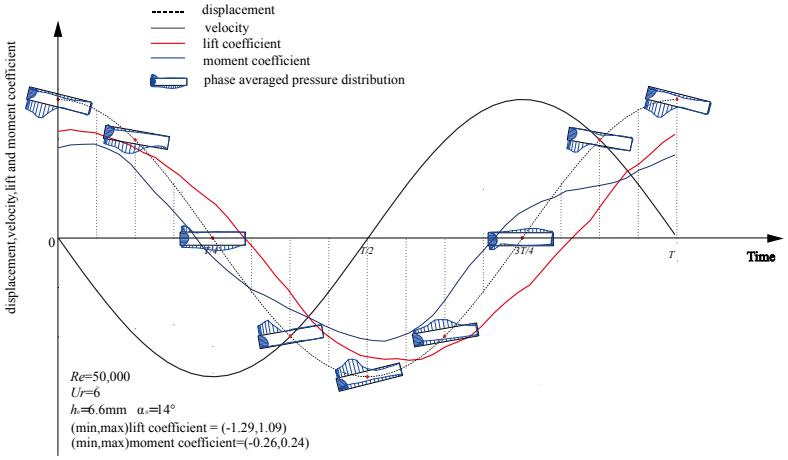

Fig. 21 Spatial-temporal C_P distributions around the surface of the rectangular cylinder at Ur=6. (a) h_0=6.6mm (b) α_0=14° (c) h_0=6.6mm, α_0=14° (positive pressure is drawn inside the cylinder, while negative outside of it)

To take a closer look at the surface pressure variation on the rectangular cylinder, 8 time steps are selected in an averaged single period of motion. Referring to practice on circular cylinders(Nikitas and Macdonald, 2015), the instantaneous pressure distribution at each time step was calculated from the ensemble averaging over many cycles. The spatial-temporal distribution of pressure coefficients for selected motion cases are reported in Fig. 21. The phase averaged distributions of single heaving (h_0=6.6mm), single pitching (α_0=14°), and coupled motion cases (h_0=6.6mm and α_0=14°) at Ur=6 are presented respectively in (a), (b) and (c). The phase averaged motion-induced lift and moment coefficients are also shown for comparisons and in support of the previously presented PDFs.

From Fig. 21 (a), the pressure distribution around the cylinder shows little variation during the whole process of the heaving motion. With the nearly symmetric distribution of pressure about the long axis of the cylinder, it can be seen that vortices keep developing around the cylinder in one pattern. This gives little chance for the occurrence of a secondary vortex shedding mechanism, substantiating probably the lack of higher harmonics observed in Fig. 11. One should also note the non-uniform lag between the motion and the lift and moment coefficients. When the cylinder is pitching at α_0=14°, the phase averaged pressure distribution varies substantially at each time step within a motion cycle. The flow separates at the leading edge corner and reattaches on both the top and bottom surface of the cylinder, because a local maximum for the pressure coefficient is detected on both sides. Local maximum of C_P appearing near the trailing edge is an indication of a secondary vortex process, as previously noted in the the flow visualization of rectangular cylinders with a positive angle of attack (Mannini et al, 2010). The position of the reattachment point is also moving forward and backward on the surface of the cylinder, which implies complex vortex development patterns for the oscillating cylinder. However, the interaction between the flow and the bluff body is influenced by many factors.

Reynolds number and oscillating frequency of the cylinder would both have an effect on the vortices around the cylinder. This paper focuses on the effects of amplitudes, so that the other effects (e.g. of frequency) will be discussed in a future paper.

For Fig. 21 (c), the pressure distribution during the oscillating process is similar to the single pitching case (Fig.21 (b)), something that can be also validated by the similarity in the mean reattachment point behavior as identified in 4.1. Now it can be noticed that positive pressures appear near the trailing edge in both sides of the cylinder. Comparing with the single pitching case with similar pitching amplitude, this could only be caused by the addition of the heaving motion. This would reflect a slightly different vortex development pattern, and it could be adopted to explain the inconsistent spectral characteristics for higher harmonics with respect to the single pitching cases.

Obviously, coupled motion cases would vary with different phase lag between the pitching and heaving motion. Therefore more comprehensive experimental study considering the phase lag shall be conducted in the future to reveal the nature of vortex development in the lag-varying coupled motion cases.

4.3 POD mode of the pressure distribution

According to sections 4.1 and 4.2, the closer the reattachment point to the leading edge, the more space there is for vortices to grow continuously. With further development of vortices, a secondary vortex, which is thought to be related with the generation of higher harmonics in motion-induced forces, would appear. The appearance of higher harmonics indicates that energy content spills in higher order complex variation patterns. The proper orthogonal decomposition (POD) has gained recognition for understanding the underlying mechanisms in fluid mechanics (Pigolotti et al, 2014). So it is herein adopted to analyse the fluctuating pressure (mean part removed) around the rectangular cylinder in order to investigate the flow mechanisms underlying the variation of motion-induced forces.

After conducting the POD analysis for heaving, pitching and coupled motion at U_r=6, the distribution of cumulative energy proportion for 60 modes is shown in Fig. 22. The result from the equivalent stationary model is also drawn (in solid line) in the figure for comparison. For the heaving motion case, the energy contribution of the 1st POD mode approaches 10% with little variation regardless of the heaving amplitude; this value is almost half of the equivalent one in the stationary case. For pitching, the contribution of the lower POD modes increases considerably when comparing to the stationary state for both the torsional amplitudes of 8° and 14° . The proportion of the 1st POD mode for the torsional amplitudes of 2°, 8° and 14° gradually increases from below the stationary case value to almost double this.

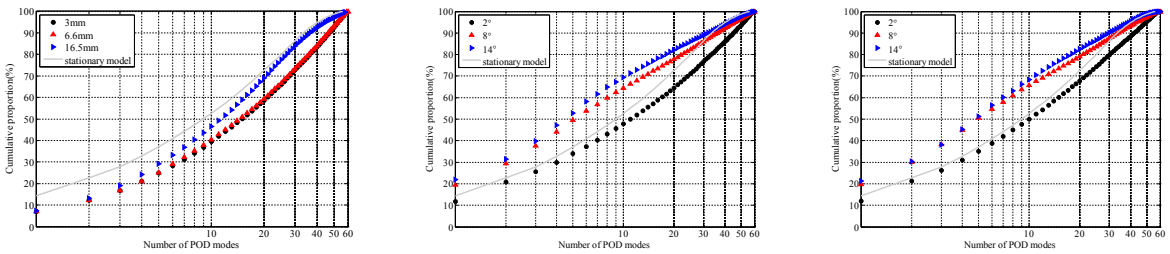

(a) heaving motion (b) pitching motion (c) coupled motion h_0=6.6mm

Fig. 22 Cumulative energy proportion of the POD modes

The path of the cumulative energy proportion for the coupled motion case is almost identical to the pitching motion case, therefore the focus will be put only on the POD modes recovered for the pitching scenario. In Fig. 23, the first 3 POD modes at α_0=2°, 8° and 14° are presented in terms of their spatial distribution. The mean and r.m.s. pressure distribution at the corresponding torsional amplitude are also drawn for comparison. It can be seen that, although the mean and r.m.s. pressure distributions are close to symmetric in all cases (as expected), the 1st order POD modes at all

amplitudes are of antisymmetric nature. By contrast, the 2nd and 3rd order POD modes are distributed either symmetrically or antisymmetrically. In particular, the 2nd order POD mode does not have monotonic behaviour. Its participation fraction rises until the amplitudes becomes α_0=8° keeping to this point an antisymmetric distribution for the top and bottom faces. For α_0=14° the participation contribution reduces marginally and its shape becomes antisymmetric. The behaviour of the 3rd POD mode is quite similar to the 2nd one, even though the shape for 14° is less asymmetric. The significant increase of the 1st POD mode participation, differently to the higher modes that slightly vary the energy regardless of pitching amplitude, should be due to a magnification of the vortex detachment mechanism for larger angles of attack. The results compare well with previous studies on POD analyses for 5:1 rectangular cylinders for the case of stationary cylinders (Bruno et al, 2010; Pigolotti et al, 2014; Ricci et al, 2017). Particularly, the participation fraction values are very close, with minimal differences that may be associated to turbulence intensity (for the effect of turbulence intensity see Ricci et al, 2017) and pressure taps layout.

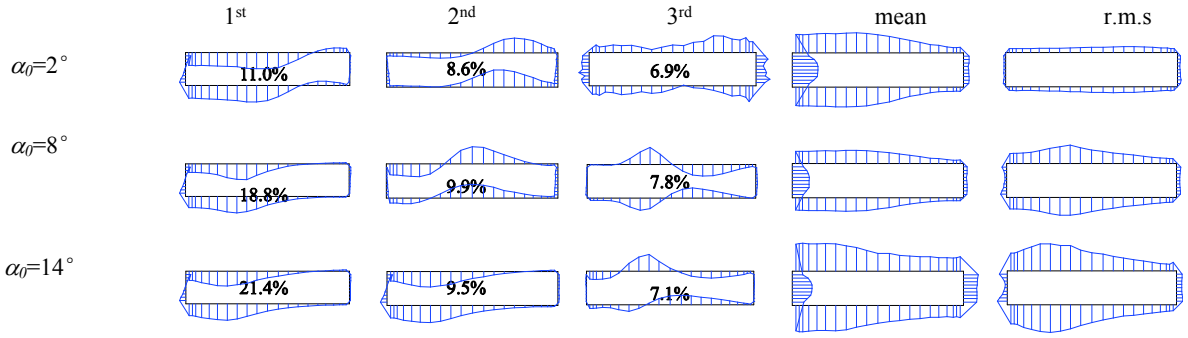

Fig. 23 First three POD modes and mean and r.m.s. distributions of pressure coefficients at different torsion motion amplitude (single pitching, U_r=6). The number indicated in each order of POD mode stands for the relevant participation proportion among all modes.

4.4 Discussion on the instantaneous angle of attack

Referring to the analysis of bridge decks (Diana et al, 2008; Diana et al, 2010), the nonlinear motion-induced force model conforms to the hypothesis that aeroelastic forces are functions of the instantaneous angle of attack $\psi(t)$. This means that equal amplitudes of instantaneous angle of attack would result in the same motion-induced force characteristics. This was validated by Diana et al (2010) for certain bridge decks, although the conjecture of this being applicable also for the bluff 5:1 rectangular cylinder was never previously assessed.

Neglecting the turbulence influence of the incoming flow, the instantaneous angle of attack for the motion cases studied in this paper can be expressed by

$$\psi(t) = \theta_0 + \alpha(t) + \tan^{-1}\left(-\frac{b\dot{\alpha} + \dot{h}}{U}\right) \tag{10}$$

where θ_0 is the initial angle of attack, b is the half-width of the cylinder (i.e. 0.5B), U is the velocity of the incoming smooth flow, and $\dot{\alpha}$, $\dot{h}$ denote the amplitude of the pitching and heaving time derivatives respectively. In the general case of coupled motion, there would be in general a phase lag □ between the pitching and heaving motions, such that the relative heaving motion displacement could be represented by

$$h(t) = h_0 \cos(2\pi f_h - \phi) \tag{11}$$

For the previously described motion cases, the amplitudes of instantaneous angle of attack $\psi(t)$, calculated by Eq. (10), are listed in Table 1.

Table 1 Amplitude of instantaneous angle of attack for different cases of motion (U_r=6)

Motion type	Motion amplitude	Amplitude of $\psi(t)$
Single heaving	h_0=3mm	0.36°
	h_0=6.6mm	0.79°
	h_0=16.5mm (case 2)	1.97°
Single pitching	α_0=2° (case 1)	2.30°
	α_0=8°	9.18°
	α_0=14°	16.01°
Coupled motion h_0=6.6mm (ϕ=0°)	α_0=2° (case 3)	2.78°
	α_0=8°	9.60°
	α_0=14°	16.42°

It can be seen that the single pitching motion of α_0=2° (case1), single heaving motion of h_0=16.5mm (case 2) and coupled motion of h_0=6.6mm, α_0=2° (case3) share very similar amplitudes of $\psi(t)$ close to 2°. In 3.3, it was shown that 1st order motion harmonics dominate the spectrum of motion-induced forces for all of cases 1 to 3, with minimal (case 1, 3) to zero (case 2) higher harmonics. For the PDFs of these three cases, significant differences can be found depending on whether heaving, pitching or coupled motion is applied. PDFs of lift and moment for the single heaving motion are close to a Gaussian distribution, while cases 1 and 3, involving pitching, present patterns closer to a bimodal distribution. Such differences are most probably linked to different flow patterns. As a matter of fact, it was confirmed in 4.1 that the location of the reattachment point varies a lot between case 2 (x/B=0.38) and cases 1 and 3 (x/B=0.25). All these differences indicate that the same amplitude of instantaneous angle of attack would not result to the same characteristics of motion-induced force. Though not explicitly presented, discrepancies in spatio-temporal pressure distributions and their associated POD modes (as previously shown for instance in Fig. 21 to Fig. 23) are also found between these three cases.

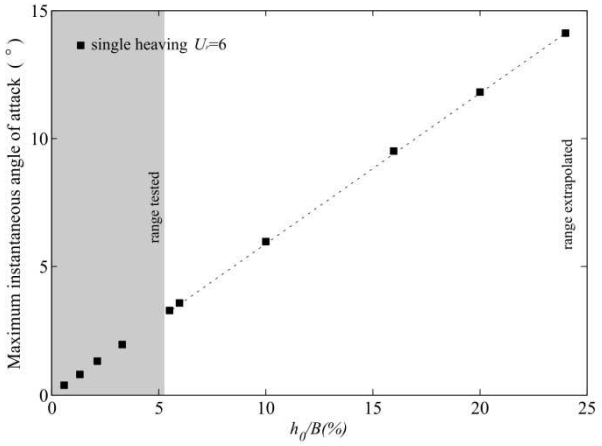

Fig. 24 Amplitude of instantaneous angle of attack for heaving motion

During the experiments, the heaving amplitude ratio h_0/B didn't exceed 5.5%, which corresponds to very low amplitudes of instantaneous angle of attack $\psi(t)$, especially when compared to the pitching motion cases. From Fig. 24, it can be seen that the amplitude of $\psi(t)$ would reach about 14° when h_0/B=25%. With such large values of $\psi(t)$, the flow field around the oscillating rectangular cylinder can be conjectured to vary beyond the currently studied heaving cases, giving rise to more complex phenomena. It should also be mentioned that there was no phase lag considered for the pitching and heaving motions during the coupled test scenarios. Evidently more research on the effects of phase

lag together with larger amplitudes of heaving should be examined in the future to further enlighten the motion-induced force amplitude dependence proposed and identified herein.

5. Conclusion

Results of a comprehensive experimental investigation on the effects of motion amplitude on motion-induced forces of a 5:1 rectangular cylinder were presented and discussed within this paper. Key conclusions deriving from the study include:

1) The torsional amplitude has a considerable influence on the flutter derivatives, especially A_2^*. Indicatively, higher torsional amplitudes would lead to lower values of A_2^* at the same reduced velocities.

2) Increased high order harmonics of the motion appear within the PSDs of motion-induced lift and moment. Such behavior would amplify for the single pitching and coupled motion cases, when the pitching amplitude exceeds 8° and 5° respectively. Variation of the heaving amplitude does not lead to similar considerable high order harmonic force components. Additionally larger torsional amplitudes lead the PDF of motion-induced force to acquire bi-modal attributes, thus becoming associated to different flow patterns.

3) By analyzing the mean and r.m.s. of the spatially distributed pressures, it is found that the reattachment point moves forward to the leading edge on the surface of the cylinder at larger torsional amplitudes. This would leave more space for vortices to develop, which could also enable the formation of secondary vortices. Concerning the POD-analysis results, larger torsional amplitudes drastically change the energy contribution, leading to a "more" organized flow. This may well relate to the high order motion harmonics appearance in the pitching and coupling pitching-heaving cases particularly with large pitching amplitudes. .

4) Equal amplitudes of instantaneous angle of attack do not lead to equal magnitudes of motion-induced forces. As such, in the future more research should be focused on larger amplitudes of heaving motion and on the phase lag between imposed heaving and pitching motions.

Acknowledgement

The research described in this paper was financially supported by the National Natural Science Foundation of China (NSFC) under grant numbers 51678508, 51778547 and U143420032. The authors would like to thank Dr Long Xiong for his support during the wind tunnel tests and also the two anonymous reviewers assigned by the journal for their valuable comments and critical suggestions holistically improving the article's readability.

References

Bartoli, G., Bruno, L., Buresti, G., Ricciardelli, F., Salvetti, M.V., Zasso, A., 2008. BARC Overview Document.

Bruno, L., Fransos, D., Coste, N., Bosco, A., 2010. 3D flow around a rectangular cylinder: A computational study. Journal of Wind Engineering and Industrial Aerodynamics 98, 263-276.

Bruno, L., Salvetti, M.V., Ricciardelli, F., 2014. Benchmark on the Aerodynamics of a Rectangular 5:1 Cylinder: An overview after the first four years of activity. Journal of Wind Engineering & Industrial Aerodynamics 126, 87-106.

Chen, Z., Yu, X., Yang, G., Spencer Jr, B., 2005. Wind-induced self-excited loads on bridges. Journal of Structural Engineering 131, 1783-1793.

Cunming, M., 2007. 3D Aerodynamic Admittance Reserach of Streamlined Box Bridge Decks. Southwest Jiaotong University, Chengdu.

Diana, G., Resta, F., Rocchi, D., 2008. A new numerical approach to reproduce bridge aerodynamic non-linearities in time domain. Journal of Wind Engineering and Industrial Aerodynamics 96, 1871-1884.

Diana, G., Resta, F., Zasso, A., Belloli, M., Rocchi, D., 2004. Forced motion and free motion aeroelastic tests on a new concept dynamometric section model of the Messina suspension bridge. Journal of Wind Engineering and Industrial Aerodynamics 92, 441-462.

Diana, G., Rocchi, D., Argentini, T., Muggiasca, S., 2010. Aerodynamic instability of a bridge deck section model: Linear and nonlinear approach to force modeling. Journal of Wind Engineering and Industrial Aerodynamics 98, 363-374.

Falco, M., Curami, A., Zasso, A., 1992. Nonlinear effects in sectional model aeroelastic parameters identification. Journal of Wind Engineering and Industrial Aerodynamics 42, 1321-1332.

Fuchs, E., Masoum, M.A., 2011. Power quality in power systems and electrical machines. Academic press.

Haan, F.L., Wu, T., Kareem, A., 2016. Correlation Structures of Pressure Field and Integrated Forces on Oscillating Prism in Turbulent Flows. Journal of Engineering Mechanics 142, 04016017.

Haan Jr, F.L., 2000. The effects of turbulence on the aerodynamics of long-span bridges. University of Notre Dame.

Kareem, A., Wu, T., 2016. Bluff Body Aerodynamics and Aeroelasticity: Nonstationary, Non-Gaussian and Nonlinear Features, Advances in Fluid-Structure Interaction. Springer, pp. 3-14.

Le, T.-H., Matsumoto, M., Shirato, H., 2009. Spanwise coherent structure of wind turbulence and induced pressure on rectangular cylinders. Wind and Structures 12, 441.

Lee, T., Su, Y.Y., 2015. Surface Pressures Developed on an Airfoil Undergoing Heaving and Pitching Motion. Journal of Fluids Engineering 137, 051105.

Li, M., Li, S., Liao, H., Zeng, J., Wang, Q., 2016. Spanwise correlation of aerodynamic forces on oscillating rectangular cylinder. Journal of Wind Engineering and Industrial Aerodynamics 154, 47-57.

Lin, H., Haili, L., 2013. Nonlinear aerodynamic forces on the flat plate in large amplitude oscillation. International Journal of Applied Mechanics 5, 544-563.

Mannini, C., Marra, A.M., Pigolotti, L., Bartoli, G., 2017. The effects of free-stream turbulence and angle of attack on the aerodynamics of a cylinder with rectangular 5:1 cross section. Journal of Wind Engineering and Industrial Aerodynamics 161, 42-58.

Mannini, C., Sbragi, G., Schewe, G., 2016. Analysis of self-excited forces for a box-girder bridge deck through unsteady RANS simulations. Journal of Fluids and Structures 63, 57-76.

Mannini, C., Šoda, A., Schewe, G., 2010. Unsteady RANS modelling of flow past a rectangular cylinder: Investigation of Reynolds number effects. Computers & Fluids 39, 1609-1624.

Matsumoto, M., 1996. Aerodynamic damping of prisms. Journal of Wind Engineering & Industrial Aerodynamics 59, 159-175.

Matsumoto, M., Shirato, H., Araki, K., Haramura, T., Hashimoto, T., 2001. Spanwise Coherence Characteristics of Surface Pressure Field on 2-D Bluff Bodies. Journal of Wind Engineering and Industrial Aerodynamics 91, 155-163.

Matsumoto, M., Yagi, T., Liu, Q., Oishi, T., Adachi, Y., 2005. Effects of axial flow and Karman vortex interference on dry-state galloping of inclined stay-cables, Proceedings of the 6th International Symposium on Cable Dynamics, pp. 247-254.

Nakamura, Y., Ohya, Y., Tsuruta, H., 1991. Experiments on vortex shedding from flat plates with square leading and trailing edges. Journal of Fluid Mechanics 222, 437-447.

Nikitas, N., Macdonald, J.H., Jakobsen, J.B., 2011. Identification of flutter derivatives from full-scale ambient vibration measurements of the Clifton Suspension Bridge. Wind and Structures 14, 221-238.

587 Nikitas, N., Macdonald, J.H.G., 2015. Aerodynamic forcing characteristics of dry cable galloping at
588 critical Reynolds numbers. European Journal of Mechanics - B/Fluids 49, Part A, 243-249.

589 Noda, M., Utsunomiya, H., Nagao, F., Kanda, M., Shiraishi, N., 2003. Effects of oscillation amplitude
590 on aerodynamic derivatives. Journal of Wind Engineering and Industrial Aerodynamics 91, 101-111.

591 Parker, R., Welsh, M.C., 1983. Effects of sound on flow separation from blunt flat plates.
592 International Journal of Heat and Fluid Flow 4, 113-127.

593 Pigolotti, L., Mannini, C., Bartoli, G., 2017. Experimental study on the flutter-induced motion of two-
594 degree-of-freedom plates. Journal of Fluids and Structures 75, 77-98.

595 Pigolotti, L., Mannini, C., Marra, A.M., Bartoli, G., 2014. Time-frequency and POD analysis of the
596 experimental pressure field around a 5:1 rectangular cylinder, in: Schlunzen, K.H. (Ed.), 6th
597 International Symposium on Computational Wind Engineering, Hamburg, Germany.

598 Ricci, M., Patruno, L., de Miranda, S., Ubertini, F., 2017. Flow field around a 5:1 rectangular cylinder
599 using LES: Influence of inflow turbulence conditions, spanwise domain size and their interaction.
600 Computers & Fluids 149, 181-193.

601 Ricciardelli, F., Marra, A.M., 2008. Sectional aerodynamic forces and their longitudinal correlation
602 on a vibrating 5:1 rectangular cylinder, BBAA VI, Milano, ITALY.

603 Robertson, J.M., Wedding, J.B., Peterka, J.A., Cermak, J.E., 1978. Wall pressures of separation—
604 reattachment flow on a square prism in uniform flow. Journal of Wind Engineering and Industrial
605 Aerodynamics 2, 345-359.

606 Sarkar, P.P., Caracoglia, L., Haan, F.L., Sato, H., Murakoshi, J., 2009. Comparative and sensitivity
607 study of flutter derivatives of selected bridge deck sections, Part 1: Analysis of inter-laboratory
608 experimental data. Engineering Structures 31, 158-169.

609 Scanlan, R.H., 1978. The action of flexible bridges under wind, I: Flutter theory. Journal of Sound &
610 Vibration 60, 187-199.

611 Schewe, G., 2013. Reynolds-number-effects in flow around a rectangular cylinder with aspect ratio
612 1:5. Journal of Fluids and Structures 39, 15-26.

613 Stokes, A.N., Welsh, M.C., 1986. Flow-resonant sound interaction in a duct containing a plate, II:
614 Square leading edge. Journal of Sound and Vibration 104, 55-73.

615 Tang, Y., 2015. Nonlinear Self-excited Forces of Streamlined Box Deck and Nonlinear Flutter
616 Response. Southwest Jiaotong Univeristy, Chengdu.

617 Washizu, K., Ohya, A., Otsuki, Y., Fujii, K., 1978. Aeroelastic instability of rectangular cylinders in a
618 heaving mode. Journal of Sound and Vibration 59, 195-210.

619 Wu, T., Kareem, A., Ge, Y., 2013. Linear and nonlinear aeroelastic analysis frameworks for cable-
620 supported bridges. Nonlinear Dynamics 74, 487-516.

621 Xiong, L., 2017. Refined Flutter Analysis Of Long Span Suspension Bridge Considering Aerostatic
622 Effects And Spanwise Correlation Of The Self-Excited Forces. Southwest Jiaotong University,
623 Chengdu.

624 Xu, F., Wu, T., Ying, X., Kareem, A., 2016. Higher-Order Self-Excited Drag Forces on Bridge Decks.
625 Journal of Engineering Mechanics 142, 06015007.

626 Zhou, M., LIu, Z., Wang, B., 2003. Suspension Bridge Handbook(in Chinese). China
627 Communications Press, Beijing, China.

628